Trade-off between NO_x storage capacity and sulfur tolerance on Al_2O_3/ZrO_2/TiO_2–based $DeNO_x$ catalysts

Zafer Say[a], Oana Mihai[b,c], Merve Kurt[a], Louise Olsson[b,*], Emrah Ozensoy[a,d,**]

[a] Department of Chemistry, Bilkent University, 06800 Ankara, Turkey
[b] Chemical Engineering, Competence Centre for Catalysis, Chalmers University of Technology, SE-412 96 Göteborg, Sweden
[c] Department of Petroleum Processing Engineering and Environmental Protection, Petroleum-Gas University of Ploiesti, 39 Bucuresti Blvd., 100680 Ploiesti, Romania
[d] UNAM-National Nanotechnology Center, Bilkent University, 06800, Ankara, Turkey

ARTICLE INFO

ABSTRACT

Al_2O_3/ZrO_2/TiO_2 (AZT) ternary mixed oxides functionalized with Pt and BaO were synthesized in powder and monolithic forms and were utilized in NO_x Storage Reduction/Lean NO_x Trap (NSR/LNT) catalysis as novel catalytic materials. Adsorption of NO_x and SO_x species and their interactions with the catalyst surfaces were systematically investigated *via in-situ* FTIR technique revealing different NO_x coordination geometries governed by the presence and the loading of BaO in the powder catalyst formulation. While BaO-free Pt/AZT stored NO_x as surface nitrates, BaO incorporation also led to the formation of bulk-like ionic nitrate species. NO_x adsorption results obtained from the current Temperature Programmed Desorption (TPD) data indicated that NO_x Storage Capacity (NSC) was enhanced due to BaO incorporation into the powder catalyst and NSC was found to increase in the following order: Pt/AZT < Pt/8BaO/AZT < Pt/20BaO/Al_2O_3 < Pt/20BaO/AZT. Increase in the NSC with increasing BaO loading was found to be at the expense of the formation of bulk-like sulfates after SO_x exposures. These bulk-like sulfates were observed to require higher temperatures for complete regeneration with $H_2(g)$. Catalytic activity results at 473 K and 573 K obtained *via* flow reactor tests with monolithic catalysts suggested that Pt/AZT and Pt/8BaO/AZT catalysts with stronger surface acidity also revealed higher resistance against sulfur poisoning and superior SO_x regeneration in spite of their relatively lower NSC. Monolithic Pt/20BaO/AZT catalyst revealed superior NSC with respect to the conventional Pt/20BaO/Al_2O_3 benchmark catalyst at 573 K after sulfur regeneration. On the other hand, this trend was reversed at high-temperatures (*i.e.* 673 K). Preliminary results were presented demonstrating the enhancement of the high-temperature NSC of AZT-based materials by exploiting multiple NO_x-storage components where BaO functioned as the low/mid-temperature NO_x-storage domain and K_2O served as the high-temperature NO_x storage domain. Enhancement in the high-temperature NO_x-storage in the BaO-K_2O multiple storage domain systems was attributed to the formation of additional thermally stable bulk-like nitrates upon K_2O incorporation.

1. Introduction

Steady growth of the world population and increasing industrialization of societies cause a constant increase in energy demand. Increasing use of fossil fuels to satisfy the rising global energy demand results in elevated levels of air pollution in both developing and developed countries alike [1]. NO_x emissions from mobile sources have serious destructive effects on the atmosphere, global ecosystem and particularly on the human health. Therefore, automotive industry must constantly improve novel catalytic abatement technologies to minimize exhaust emission levels by designing novel catalytic materials.

In 1990's, Toyota Motor Company introduced a novel technology for diesel engine tail pipe emission control systems operating in a cyclic mode (*i.e.* lean and rich), called NO_x storage and reduction (NSR) or Lean NO_x Trap (LNT) technology [2]. Conventional after-treatment technology for diesel engine emission systems is the Selective Catalytic Reduction (SCR) technology which selectively reduces NO_x emissions with additional reducing agents such as urea/NH_3 and/or HC in a non-cyclic manner under continuous lean regime. The LNT can be combined in the tail pipe with diesel oxidation catalysts (DOC) and diesel particulate filters (DPF), which can eliminate HC/CO emissions and particulate matter, simultaneously [3,4]. Tail pipe systems utilizing LNT and SCR systems at the same time may reduce NO_x emissions and also eradicate ammonia slip as recently demonstrated by Daimler AG [5]. In

---

this dual-bed catalytic architecture, LNT catalyst is placed upstream in the tail pipe before the SCR catalyst. LNT catalyst serves as the primary NO_x storage/reduction material and is followed by the SCR catalyst. SCR catalyst converts the residual NO_x slipping into the atmosphere during the lean phase of LNT and simultaneously utilizes the NH_3 generated during the LNT rich phase as an external reducing agent in the SCR process [6,7].

SCR and NSR after treatment systems for diesel applications are known to have various drawbacks associated with coke deposition, thermal aging and sulfur poisoning [3,4,8–11]. The temperature in the tail pipe systems can reach high levels for the removal of particulate matter and sulfur regeneration. Thus, catalytic materials are typically exposed to harsh operational conditions resulting in sintering of active sites/promoters/catalytic support materials and loss of specific surface area (SSA) and functionality [12]. Furthermore, since acidic $NO_2(g)$ and $SO_2(g)$ adsorbates compete for similar adsorption sites on the catalyst surface, SO_x species gradually accumulate over the BaO NO_x-storage components and form $BaSO_4$ which is thermodynamically more stable than $Ba(NO_3)_2$ and $BaCO_3$ diminishing the NSC of the LNT catalyst [13–15].

Hence, surface chemistry and the composition of the LNT catalytic materials need to be tailored at the nanometer scale in order to enhance their NSC, thermal stability and sulfur poisoning resistance. For instance, in former studies, CeO_2 promotion was found to enhance NO_x reduction efficiency under rich conditions while improving the SO_x regeneration capability [8,16–18]. We have also demonstrated that TiO_2 promotion of BaO/Al_2O_3 mixed oxides can lead to SO_x release from a poisoned LNT catalyst at significantly lower temperatures than that of the unpromoted catalyst [9,19]. However, we have also reported that BaO can diffuse into the TiO_2 domains at temperatures higher than 500 °C due to the strong interaction between TiO_2 and BaO domains, forming complex $BaTiO_x$ mixed oxides causing thermal aging and deactivation along with a loss in NSC [19–21]. Platinum group metals (PGM) such as Pt, Pd, and Rh serve as the active redox sites in LNT systems. Besides the PGM active sites, nature and the loading of the NO_x storage domains and the type of the metal oxide support materials are other critical factors affecting the overall performance and stability of LNT catalysts [22–29].

Novel catalytic mixed oxide architectures can be synthesized with improved material properties by utilizing the well-known stabilizing influence of ZrO_2 acting as a diffusion barrier between BaO and TiO_2 domains [30–34]. Along these lines, in a recent publication, we reported that incorporation of BaO to the $Pt/ZrO_2/TiO_2$ catalyst leads to the formation of ordered $BaTiO_3$ and $ZrTiO_4$ phases rendering a drastic drop in the SSA of the catalytic material from 250 m^2/g to 24 m^2/g. On the other hand, in the $Al_2O_3/ZrO_2/TiO_2$ (AZT) quaternary mixed oxide system functionalized with BaO, Al_2O_3 was found to act as a diffusion barrier in between BaO and TiO_2 domains of the Pt/BaO/AZT catalyst. This effect leads to the formation of a highly amorphous and thermally stable structure at elevated temperatures as high as 973 K [22]. AZT-based LNT catalysts such as Pt/Rh/Ba/K/AZT and titanium doped-AZT have also been investigated by others in the literature [35,36]. Zou *et al.* studied the influence of the mass ratio of $Al_2O_3:ZrO_2-TiO_2$ components on the catalytic performance of the Pt/K/AZT system and reported that a mass ratio of 1:1 revealed the best performance after sulfur poisoning [37]. A recent publication by Toyota Motor Company also investigated the nature of BaO domains on the ZrO_2/TiO_2 and Al_2O_3 oxides by means of *in-situ* FTIR studies [38].

In the current manuscript, we focus on the NO_x/SO_x adsorption and desorption characteristics of AZT (ternary mixed oxide) and BaO/AZT (quaternary mixed oxide) systems functionalized with Pt redox active sites in comparison to a benchmark NSR/LNT catalyst (*i.e.* Pt/BaO/Al_2O_3) by means of *in-situ* Fourier Transform Infrared Spectroscopy (*in-situ* FTIR) and Temperature Programmed Desorption (TPD) techniques. In addition to the analysis of the interactions between the NO_x and SO_x species with the catalytic surfaces and their transformations under

catalytic conditions at the molecular level on powder catalysts in batch mode; we also performed quantitative catalytic performance tests using monolithic catalysts under realistic operational conditions in a flow reactor, in order to determine NSC values at different operational temperatures after sulfur poisoning and subsequent regeneration. We also provide preliminary results regarding how NSC of BaO-based AZT systems can be improved by their incorporation with K_2O. Therefore, in the current contribution, we report a holistic investigation of the AZT-based LNT catalysts consolidating surface spectroscopic investigations shedding light on the nature of the reactants/products (*e.g.* NO_x) and poisons (*e.g.* SO_x) on the catalyst surface as a function of catalyst composition and operational conditions (*e.g.* temperature) and combine these results with realistic catalytic activity/poisoning/regeneration measurements revealing the performance and durability of the currently designed catalytic architectures.

2. Experimental

2.1. Material synthesis

Detailed description of the synthesis procedures for the $Al_2O_3/ZrO_2/TiO_2$ (AZT, $Al_2O_3:ZrO_2:TiO_2$ = 50:35:15, by mass) catalyst and further information regarding all of the chemicals/gases used in the synthesis and *in-situ* characterization experiments can be found in our former reports [18,39,40]. Pt/BaO/AZT and Pt/BaO/Al catalysts were synthesized with 8 or 20 wt.% nominal BaO loadings (*i.e.* Pt/8BaO/AZT, Pt/20BaO/AZT, and Pt/20BaO/Al; respectively) and 1 wt.% nominal Pt loading. These particular BaO loadings were chosen in order to be comparable with the former reports in the literature on the conventional Pt/BaO/Al LNT catalyst, where 8 wt.% BaO loading corresponds to a nominal BaO surface coverage of *ca.* 1.0 monolayer (ML) on γ-Al_2O_3 resulting in the formation of predominantly 2D-BaO islands and small BaO particles, and higher BaO loadings (*i.e.* 20 wt.%) with a nominal surface coverage greater than 1.0 ML leads to the formation of mostly bulk-like 3D-BaO structures on γ-Al_2O_3 along in addition to smaller BaO particles [41]. Moreover, physically mixed hybrid catalyst was prepared by mixing 50 wt.% of each Pt/5.4 K_2O/AZT and Pt/8BaO/AZT.

2.2. In-situ FTIR and TPD measurements

Transmission mode *in-situ* FTIR measurements were performed in a custom-designed batch-type spectroscopic reactor coupled to an FTIR spectrometer (Bruker Tensor 27) and a quadruple mass spectrometer (QMS, Stanford Research Systems, RGA 200) for TPD analysis [39]. All of the FTIR spectra were acquired at 323 K using the powder form of the catalysts.

Stepwise NO_x adsorption experiment series were performed by flushing the material surfaces with 1.0 Torr of $NO_2(g)$ for 5 min and subsequent annealing to 973 K with a 12 K/min heating rate under vacuum in order to remove all of the adsorbed contaminants and water on catalyst surfaces. Then, material surfaces were gradually exposed to $NO_2(g)$ at 323 K in a stepwise fashion from low to higher pressures where each exposure step took 1 min. Finally, surface saturation was achieved *via* the introduction of 5.0 Torr $NO_2(g)$ over the catalyst surfaces for 10 min at 323 K followed by evacuation to a pressure lower than 10^{-2} Torr.

In-situ CO adsorption experiments were carried out using FTIR technique by exposing the fresh and spent catalyst surfaces to 10.0 Torr of CO(g) for 10 min at 323 K. Prior to analysis of fresh catalyst (calcined powder), material was pre-treated by exposing to 10.0 Torr of H_2 at 773 K for 10 min. CO adsorption experiment was also applied to the spent catalyst in the powder form that was scraped from the spent monolith after poisoning and high temperature regeneration.

Sulfur desorption/regeneration characteristics of each material was investigated by exposing the pre-poisoned (2.0 Torr SO_2 + O_2 gas

mixture, $SO_2:O_2 = 1:10$, at 673 K for 5 min, SO_2 purity > 99%, Air Products, O_2 purity > 99.999%, Linde GmbH) catalyst surfaces to 15.0 Torr of H_2 (H_2 purity > 99.999%, Linde GmbH) at 323 K. Next, catalyst surfaces were annealed at 773 K in the presence of H_2 for 5 min. Finally, the catalysts were cooled to 323 K in the reducing gas environment and FTIR spectra were acquired.

NO_x storage and desorption on powder catalysts were also subsequently followed by TPD analysis. In TPD runs, NO_2-saturated catalysts were heated up to 973 K with a linear heating rate of 12 K/min in vacuum. FTIR spectra of the corresponding surfaces were also recorded before and after the TPD experiments.

2.3. Catalytic reactions

NO_x storage characteristics of the synthesized materials before and after sulfur poisoning and regeneration were studied in detail using monolithic samples in a flow reactor system. The monoliths (length = 20 mm, diameter = 21 mm, cell density of 400 cpsi) were then wash-coated with the powder catalysts of Pt/AZT, Pt/8BaO/AZT, Pt/20BaO/AZT and Pt/20BaO/Al. Details regarding the monolith preparation can be found elsewhere [40]. The washcoat consisted of 5 wt. % boehmite as a binder and 95 wt.% powder catalyst. The washcoated monoliths were finally calcined at 873 K for 2 h.

The sulfur poisoning, regeneration and the storage/reduction cycles were carried out in a horizontally mounted quartz tube flow reactor [40]. The temperature was regulated using a thermocouple placed about 10 mm in front of the monolith, and in addition the temperature was measured by another thermocouple in a center channel. The inlet gas feed, including water vapor, was regulated using several Bronkhorst mass flow controllers and a CEM system (controlled evaporation and mixing system from Bronkhorst Hi-Tech). All lines were heated and maintained at 473 K in order to prevent water condensation. The gases coming out of the reactor were analysed by a gas phase FTIR spectrometer (MKS Instruments, MultiGas 2030) with the gas cell heated to 464 K.

The calcined monoliths were first degreened at 923 K in order to stabilize the samples. During degreening, the samples were exposed to 1% H_2 for 30 min at 923 K; then the samples were flushed with Ar for 5 min at 923 K, and then using an additional gas mixture (500 ppm NO, 5% O_2, 5% CO_2, 5% H_2O), balanced with Ar at 923 K for 2 h. The stability of the samples was examined by conducting experiments at 573 K with eleven successive lean/rich cycles (7 cycles with NO in the feed and 4 cycles with NO_2, in the presence of 5% CO_2, 5% H_2O, and 10% O_2) (for lean step during 4 min) and 1% H_2 (for rich step during 1 min). The cycles described above were denoted in this study as a single set of stability test and before each stability test a pre-treatment, described in the following section, was performed. This set was repeated three times for Pt/20BaO/Al, Pt/20BaO/AZT and Pt/AZT. Moreover, Pt/8Ba/AZT catalyst was subjected to three additional stability sets, since it was not completely stable after three sets.

After the stability tests, the samples were subjected to NO_x experiments where successive lean/rich cycles (seven cycles with NO in the feed and four cycles with NO_2) at three different temperatures of 673 K, 573 K and 473 K were performed. Before each experiment at each temperature the catalysts were pretreated at 773 K with 1% H_2, 5% CO_2 and 5% H_2O for 15 min, which was followed by exposing the sample to 5% CO_2, 5% H_2O and Ar for 5 min and finally an oxidation step with 5% O_2, 5% CO_2 and 5% H_2O for 15 min.

SO_2 poisoning was investigated by exposing the samples to sulfur-containing gas mixture where lean and rich cycles were alternated. For the SO_2 poisoning tests, the temperature was decreased to 573 K after pre-treatment at 773 K and ten successive lean/rich cycles were conducted according to the following procedure: (1) lean cycle: 30 ppm SO_2, 500 ppm NO, 10% O_2, 5% CO_2 and 5% H_2O for 4 min; (2) rich cycle: 30 ppm SO_2, 500 ppm NO, 1% H_2, 5% CO_2 and 5% H_2O for 1 min. Thereafter, the same lean-rich cycling was repeated at the respective

temperature without sulfur to study the activity of the catalyst after sulfur poisoning. It should be noted that pre-treatment was always conducted before each experiment at each temperature.

Sulfur regeneration of the catalysts was also investigated and the samples were regenerated at 773 K and 973 K, respectively, in a gas mixture of 1% H_2, 5% CO_2 and 5% H_2O for 1 h. After the regeneration, the samples were pre-treated (as reported above) and subjected to seven lean/rich cycles at 573 K contained NO + O_2 + CO_2 + H_2O (during lean) and NO + H_2 + CO_2 + H_2O (during rich), followed by four cycles with NO_2. For all catalytic reactions, flow rate was set to 3 L/min.

NH_3-TPD measurements were performed in a Setaram Sensys Digital Scanning Calorimeter (DSC), combined with an Hiden HPR-20 QUI mass-spectrometer using powder samples (about 60 mg). After degreening of the powder at 923 K (0.9% H_2 for 30 min; Ar 5 min; 474 ppm NO, 4.5% O_2, 4.8% CO_2 for 2 h) and pre-treatment (8% O_2 for 30 min and 0.9% H_2 for 1 h) the catalyst was exposed to 2000 ppm ammonia at 323 K for 8 h. Next, the samples were treated with Argon for 30 min, and the temperature was increased to 1073 K with a heating rate of 5 °C/min in the presence of Ar (g) flow. Further details regarding the NH_3-TPD measurements can be found elsewhere [40].

3. Results and discussion

3.1. NO_x adsorption and desorption nature of AZT-based NSR/LNT materials

Fig. 1 illustrates the *in-situ* FTIR spectra corresponding to $NO_2(g)$ adsorption at 323 K on (a) Pt/AZT, (b) Pt/8BaOAZT, (c) Pt/20BaO/AZT and (d) Pt/20BaO/Al_2O_3 starting from low pressures up to saturation (5.0 Torr NO_2 for 10 min). Each material exhibits highly convoluted features in the spectral range of 1800–1000 cm^{-1} including well-known oxide coordinated nitrite and nitrate functional groups reported in literature as well as in our former studies [18,20,39,42–46].

In Fig. 1a, there are five main vibrational stretchings located at 1640, 1582, 1561, 1283 and 1238 cm^{-1} on BaO-free Pt/AZT material. While features at 1640 and 1238 cm^{-1} can be attributed to bridging nitrates, other three frequencies at 1582/1283 and 1561 cm^{-1} are associated with bidentate and monodentate nitrates; respectively [39,47]. It is worth mentioning that highly convoluted spectral line characteristics renders assignment of nitrate/nitrite features rather difficult. Incorporation of BaO domains leads to a different spectral line shape as demonstrated in Fig. 1b and c for Pt/8BaO/AZT and Pt/20BaO/AZT; respectively. Fig. 1b–d shows that NO_x adsorption on each material generates six main vibrations located at *ca.* 1628, 1570, 1480, 1436, 1324 and 1234 cm^{-1}. In addition to the surface nitrate/nitrite groups, formation of bulk/ionic type of nitrate groups which are apparent by the features located at *ca.* 1480, 1437 and 1322 cm^{-1} are observed as well. For all of the sample surfaces in Fig. 1, it is apparent that NO_2 molecules are initially adsorbed as nitrites evident by the feature located at 1211 cm^{-1} and are subsequently oxidized to nitrate functional groups.

It is also visible in Fig. 1b and c that the absorbance intensity of the spectrum corresponding to NO_x-saturated Pt/20BaO/AZT (top-most red spectra in Fig. 1c) is clearly higher than that of Pt/8BaO/AZT (Fig. 1b). These findings imply a higher amount of NO_x adsorption on Pt/20BaO/AZT as compared to Pt/AZT and Pt/8BaO/AZT at 323 K. However, deduction of quantitative information regarding adsorbate coverages solely from FTIR absorption intensities could be misleading due to variations in IR absorption cross sections. Thus, a more accurate and a quantitative comparison of NSC was also performed *via* TPD experiments on powder catalysts in batch mode and flow-mode reactor studies on monolithic catalysts which will be described in the upcoming sections demonstrating good correlation between batch-mode and flow-mode experimental findings.

NO_x adsorption and desorption properties of the synthesized powder catalysts *via in-situ* FTIR analysis in batch-mode yield mostly
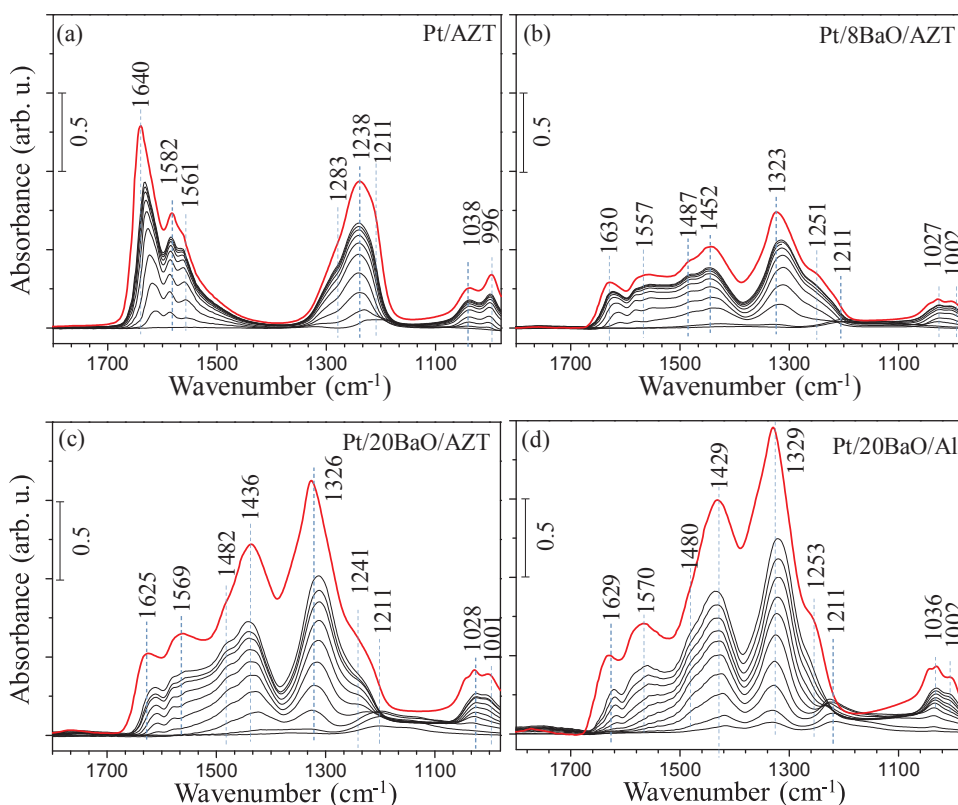
Fig 1. FTIR spectra corresponding to the stepwise $NO_2(g)$ adsorption at 323 K on (a) Pt/AZT, (b) Pt/8BaO/AZT, (c) Pt/20BaO/AZT and Pt/20BaO/Al$_2$O$_3$ surfaces. The bold (red) spectrum in each panel corresponds to the NO_x-saturated surfaces (*i.e.* after 5.0 Torr $NO_2(g)$ for 10 min at 323 K). (For interpretation of the references to colour in this figure legend, the reader is referred to the web version of this article.)

qualitative information. Hence, FTIR experiments were complemented with batch-mode TPD experiments in order to gather semi-quantitative information regarding the total NO_x adsorption quantities and thermal stabilities of adsorbed nitrate/nitrite species as well as their decomposition pathways.

Prior to TPD experiments, materials were saturated with 5.0 Torr $NO_2(g)$ for 10 min at 323 K, followed by vacuum annealing up to 973 K. Fig. 2a–d illustrates the TPD profiles obtained after $NO_2(g)$ adsorption over Pt/AZT, Pt/8BaO/AZT, Pt/20BaO/AZT and Pt/20BaO/Al materials; respectively. Thermal decomposition of adsorbed nitrate species on Pt/AZT and Pt/8BaO/AZT exhibits relatively similar characteristics as shown in Fig. 2a and b; respectively. It is clear that NO desorption signal ($m/z = 30$) revealed two main desorption maxima at 645 and 740 K. Nitrate decomposition produces desorption channels of NO ($m/z = 30$), NO_2 ($m/z = 46$) and O_2 ($m/z = 32$) at low temperatures (*i.e.* 645 K), while the major desorption channels are primarily NO ($m/z = 30$) and O_2 ($m/z = 32$) for high temperatures (*i.e.* 740 K). Identical TPD experiments were also performed for the catalysts with higher BaO loadings (*i.e.* wt.% 20 BaO). Thermal decomposition of nitrate species on Pt/20BaO/AZT and Pt/20BaO/Al$_2$O$_3$ surfaces are illustrated in Fig. 2c and d; respectively. As compared to the TPD results for Pt/AZT and Pt/8BaO/AZT (Fig. 2a and b), Fig. 2c and d clearly indicates that the desorption channels related to NO ($m/z = 30$) and O_2 ($m/z = 32$) are more pronounced at higher temperatures (*i.e.* 750 K). Increase in BaO loading from 8 wt.% to 20 wt.% leads to formation of a greater extent of bulk like nitrate species which is consistent with the observation of stronger high temperature (*i.e.* 750 K) NO and O_2 desorption signals.

In addition to the mechanistic information discussed above, one can also obtain quantitative knowledge from the TPD results regarding the relative NO_x adsorption capabilities of different catalysts by integrating each of the N-related desorption channels (*i.e* N_2, NO, N_2O, and NO_2) by considering particular QMS fragmentation patterns of all of the desorbing species. More details regarding fragmentation calculations can be found elsewhere [39]. In such a semi-quantitative analysis, it is also

important to make sure that all of the NO_x species are completely removed from the surfaces at the end of TPD experiments. In order to verify this point, *in-situ* FTIR data corresponding to the surfaces before and after TPD runs were acquired as shown in the insets of Fig. 2. These *in-situ* FTIR results clearly illustrate that materials were completely regenerated after TPD experiments (*i.e.* annealing under vacuum at 973 K).

Table 1 shows the total NO_x desorption from investigated catalyst normalized by either mass or SSA of the catalysts. Calculated numbers clearly suggest that NO_x adsorption capability of Pt/AZT is only slightly affected by the addition of 8 wt.% BaO. However, a higher BaO loading (*i.e.* 20 wt.%) onto Pt/AZT leads to a drastic change where total NO_x release increased by about 58%. Another striking aspect of Table 1 is the fact that total NO_x release of Pt/20BaO/AZT is 19% higher than that of benchmark Pt/20BaO/Al$_2$O$_3$ catalyst. This latter finding clearly emphasizes the relatively better NO_x storage performance of the AZT support material in comparison to the conventional γ-Al$_2$O$_3$ support for identical Pt and BaO loadings.

Moreover, calculated NO_x adsorption quantities can also be assessed by considering their specific surface areas (SSA). SSA-normalized NO_x release values increase in the following order: Pt/AZT < Pt/8BaO/AZT < Pt/20BaO/Al$_2$O$_3$ < Pt/20BaO/AZT. Here, it should be mentioned although these results are informative, they correspond to batch mode experiments on powder catalysts where initial adsorption was performed at 323 K. Thus, for a more accurate evaluation of NSC values, flow-mode NO_x adsorption and release experiments were performed on monolithic catalysts under operationally-relevant conditions as discussed in depth in the next section.

3.2. Quantitative NSR performance analysis

In order to evaluate the NO_x storage reduction (NSR) performance of the synthesized materials under more realistic conditions in the form of wash-coated monoliths before and after exposure to SO_x as well as after SO_x regeneration at 773 and 973 K, flow reactor measurements
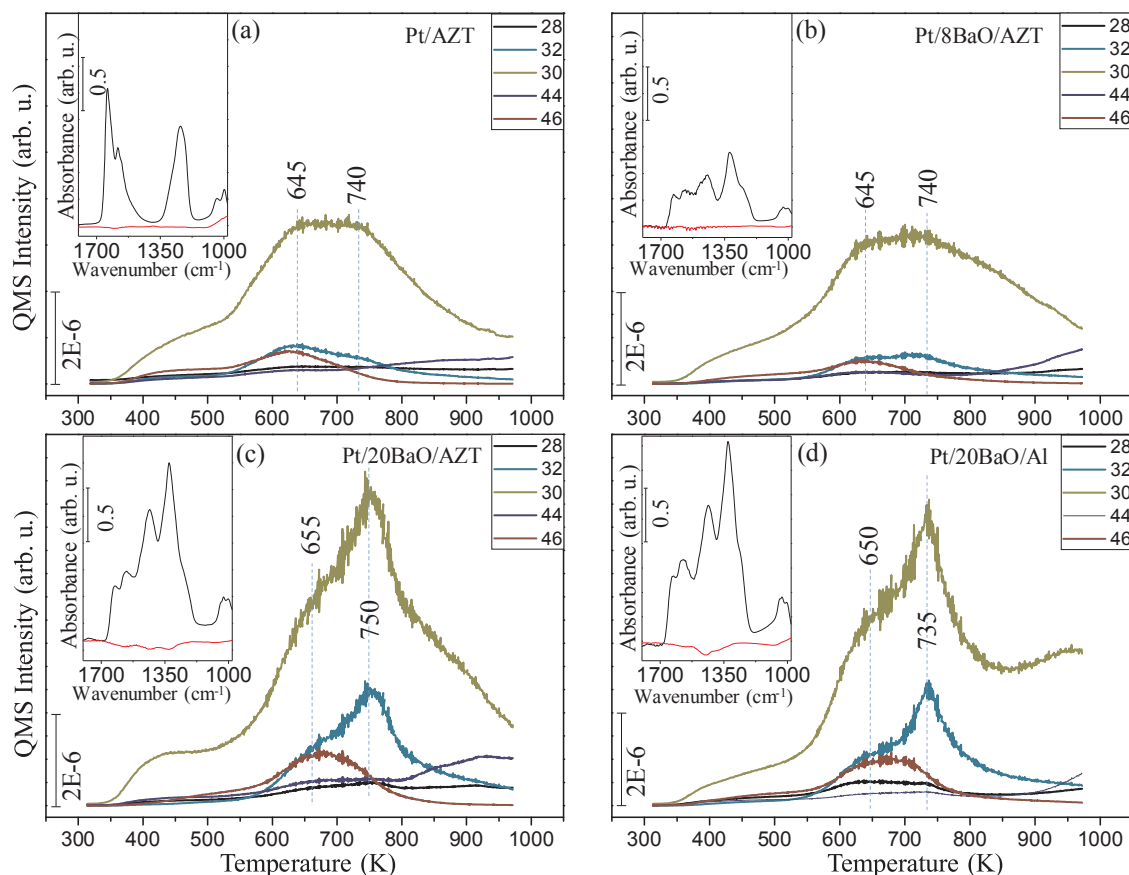
Fig. 2. TPD profiles obtained from (a) Pt/AZT, (b) Pt/8BaO/AZT, (c) Pt/20BaO/AZT and (d) Pt/20BaO/Al$_2$O$_3$ samples after saturation of each surface with 5 Torr NO$_2$(g) at 323 K for 10 min. The inset in each panel shows the *in-situ* FTIR spectra of the surfaces before (black) and after (red) TPD analysis at 323 K. (For interpretation of the references to colour in this figure legend, the reader is referred to the web version of this article.)

Table 1
Integrated NO$_x$ TPD desorption signals and corresponding SSA-normalized relative NO$_x$ release values.

Catalyst Name	Relative number of desorbed NO$_x$ species per mass of catalyst (arb. u.)	Relative number of desorbed NO$_x$ species per SSA of catalyst (arb. u.)
Pt/AZT	19	10
Pt/8BaO/AZT	22	15
Pt/20BaO/AZT	30	23
Pt/20BaO/Al	25	19

were carried out as described in the experimental section. NSC were calculated by integration of the outlet NO$_x$ concentrations with respect to the inlet concentration and the obtained NSC results are depicted in Figs. 3 and 4, for experiments conducted at 473 and 573 K, respectively.

Fig. 3 illustrates the NSC values at 473 K for fresh (F), sulfur-poisoned (S), regenerated at 773 K (R') and 973 K (R") catalysts in terms of mmol/g$_{cat}$ for Pt/AZT, Pt/8BaO/AZT, Pt/20BaO/AZT and Pt/20BaO/Al. These results clearly point out the fact that Pt/AZT and Pt/8BaO/AZT revealed superior resistance against sulfur poisoning at 473 K, where NSC values remain practically invariant for fresh, SO$_x$-poisoned and regenerated catalysts at 773 K (R'). It should be noted that the for the SO$_x$ poisoned catalyst lean-rich cycling was conducted after the sulfur poisoning in addition to pre-treatment steps conducted before each experiment at each temperature. Interestingly, high temperature regeneration of these catalysts at 973 K (R") leads to an apparent increase in NSC due to change in material morphology under the severely reducing regeneration conditions which will be discussed further in the text below.

On the other hand, increase in the loading of the basic storage domain (*i.e.* BaO) significantly alters the performance characteristics of Pt/20BaO/AZT in the presence of sulfur-poisoning (Fig. 3). Although fresh Pt/20BaO/AZT catalyst exhibits comparable NSC to the fresh Pt/AZT and fresh Pt/8BaO/AZT, its NSC is significantly influenced by the SO$_x$ exposure, resulting in *ca.* 40% decrease. Among all of the investigated materials, benchmark Pt/20BaO/Al was found to have the most severe relative attenuation in NSC upon sulfur poisoning (*i.e.* 52% loss in NSC with respect to its fresh form). Moreover, comparison of the Pt/20BaO/AZT and Pt/20BaO/Al materials provides an insight regarding the influence of the support material (AZT *vs.* Al$_2$O$_3$) on the sulfur regeneration performance. While the NSC after thermal regeneration at 773 K was found to be *ca.* 73.6% of the NSC of fresh Pt/20BaO/AZT, this was limited to only 52% for the conventional Pt/20BaO/Al benchmark catalyst. Differences in the percent regeneration capabilities of AZT and γ-Al$_2$O$_3$ supported materials after sulfur poisoning becomes even more evident after the regeneration at 973 K (Fig. 3). While Pt/20BaO/AZT catalyst could recover *ca.* 100% of its original NSC after regeneration at 973 K, Pt/20BaO/Al could only recover 76% of its NSC.

Further experiments were also carried out in order to investigate the effect of temperature on NSC as shown in Fig. 4. It is seen that NSC of BaO-free Pt/AZT decreases to some extent at 573 K as compared to that of 473 K. However, it should be noted that although NSC of fresh Pt/AZT at 573 K is almost one third of Pt/20BaO/Al, it demonstrates a striking resilience against sulfur poisoning, preserving *ca.* 96% of its original NSC at 573 K (*i.e.* 0.024 *vs* 0.022 mmol/g$_{cat}$) after poisoning. Thus, AZT support has poor NO$_x$ and SO$_x$ storage. In order to utilize the full potential of the AZT material, it should be combined with a storage component such as barium. It is also apparent that fresh Pt/20BaO/AZT
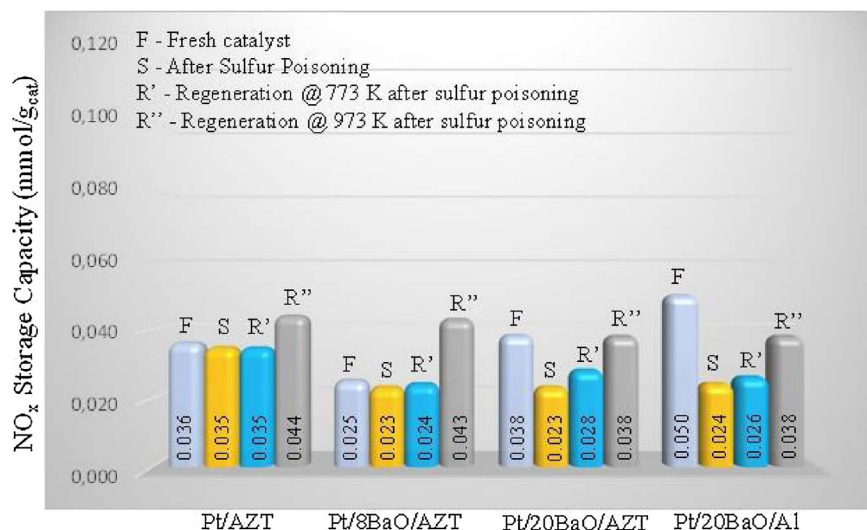
Fig. 3. NO$_x$ storage capacities (NSC) of Pt/AZT, Pt/8BaO/AZT, Pt/20BaO/AZT and Pt/20BaO/Al monolithic catalysts at 473 K obtained in a flow-reactor using an inlet gas feed of 500 ppm NO, 5% O$_2$, 5% CO$_2$, 5% H$_2$O, balanced in Ar. F = fresh, S = SO$_x$ poisoned, R' = regenerated at 773 K after SO$_x$ poisoning, and R" = regenerated at 973 K after SO$_x$ poisoning (see text for details).
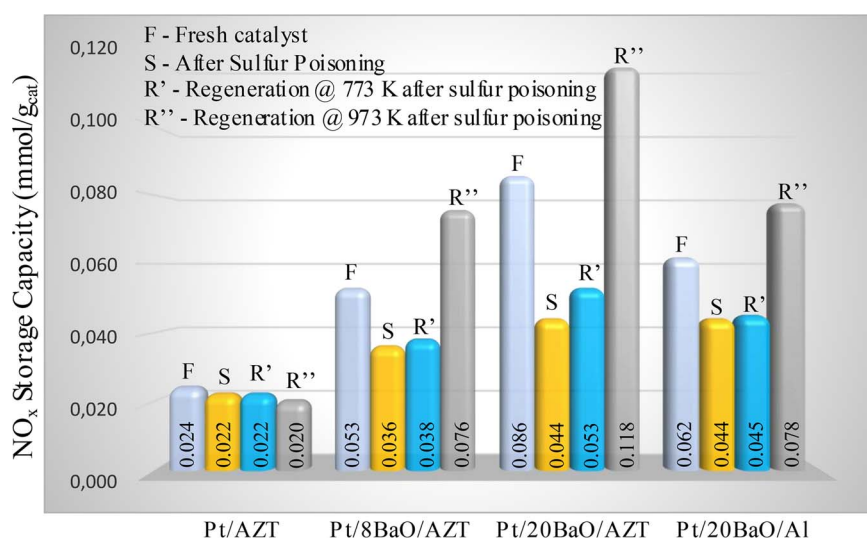

Fig. 4. NO$_x$ storage capacities (NSC) of Pt/AZT, Pt/8BaO/AZT, Pt/20BaO/AZT and Pt/20BaO/Al monolithic catalysts at 573 K obtained in a flow-reactor using an inlet gas feed of 500 ppm NO, 5% O$_2$, 5% CO$_2$, 5% H$_2$O, balanced in Ar. F = fresh, S = SO$_x$ poisoned, R = regenerated at 773 K after SO$_x$ poisoning, and R" = regenerated at 973 K after SO$_x$ poisoning (see text for details). NSC values given in this figure for 573 K are based on the data reported in one of our recent publications [40].

exhibits *ca.* 38% higher NO$_x$ storage at 573 K than that of Pt/20BaO/Al benchmark catalyst. Indeed, NSC performance of Pt/20BaO/AZT at 573 K after high temperature regeneration (R") is the highest among all of other investigated catalyst (*i.e.*52% higher than that of Pt/20BaO/Al). It should also be noted that Pt/8BaO/AZT exhibited comparable NSC at 573 K to the benchmark Pt/20BaO/Al catalyst after regeneration at 973 K.

The increase in NSC at 573 K after regeneration at 973 K (Fig. 4) deserves more attention. It is seen that regeneration at elevated temperatures under a severely reducing environment not only facilitates the sulfur regeneration, but leads to increased NO$_x$ storage, which could be due to structural changes in the materials. This can be tentatively attributed to the enhancement of the dispersion of BaO and AZT support upon high temperature regeneration. This is also in very good agreement with one of our recent reports, indicating enhanced BaO dispersion on ZrO$_2$/TiO$_2$ as compared to γ-Al$_2$O$_3$ [38]. Enhanced BaO dispersion was also demonstrated on the TiO$_2$/Al$_2$O$_3$ support material [21].

In order to shed light on the changes in Pt sintering due to aging, poisoning and regeneration, we performed *in-situ* FTIR spectroscopy experiments and followed CO adsorption characteristics of Pt sites on fresh Pt/20BaO/AZT powder directly after calcination and spent Pt/20BaO/AZT catalysts scraped of washcoat from the sulfur regenerated Pt/20Ba/AZT monolith as shown in Fig. 5. *In-situ* FTIR spectrum in
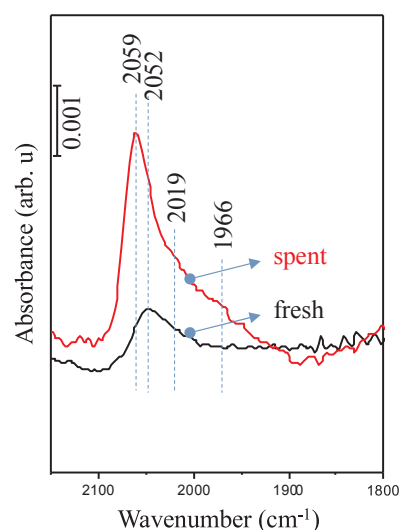
Fig. 5. *In-situ* FTIR spectra corresponding to 10 Torr CO(g) adsorption at 298 K for 10 min on fresh and spent (used in LNT, poisoned with SO$_x$ and regenerated) Pt/20BaO/AZT catalyst. Before the acquisition of the fresh catalyst spectrum, catalyst was treated with 10 Torr H$_2$(g) at 773 K for 10 min followed by cooling to 298 K and evacuation. Spent catalyst CO adsorption spectrum was acquired without further treatment.
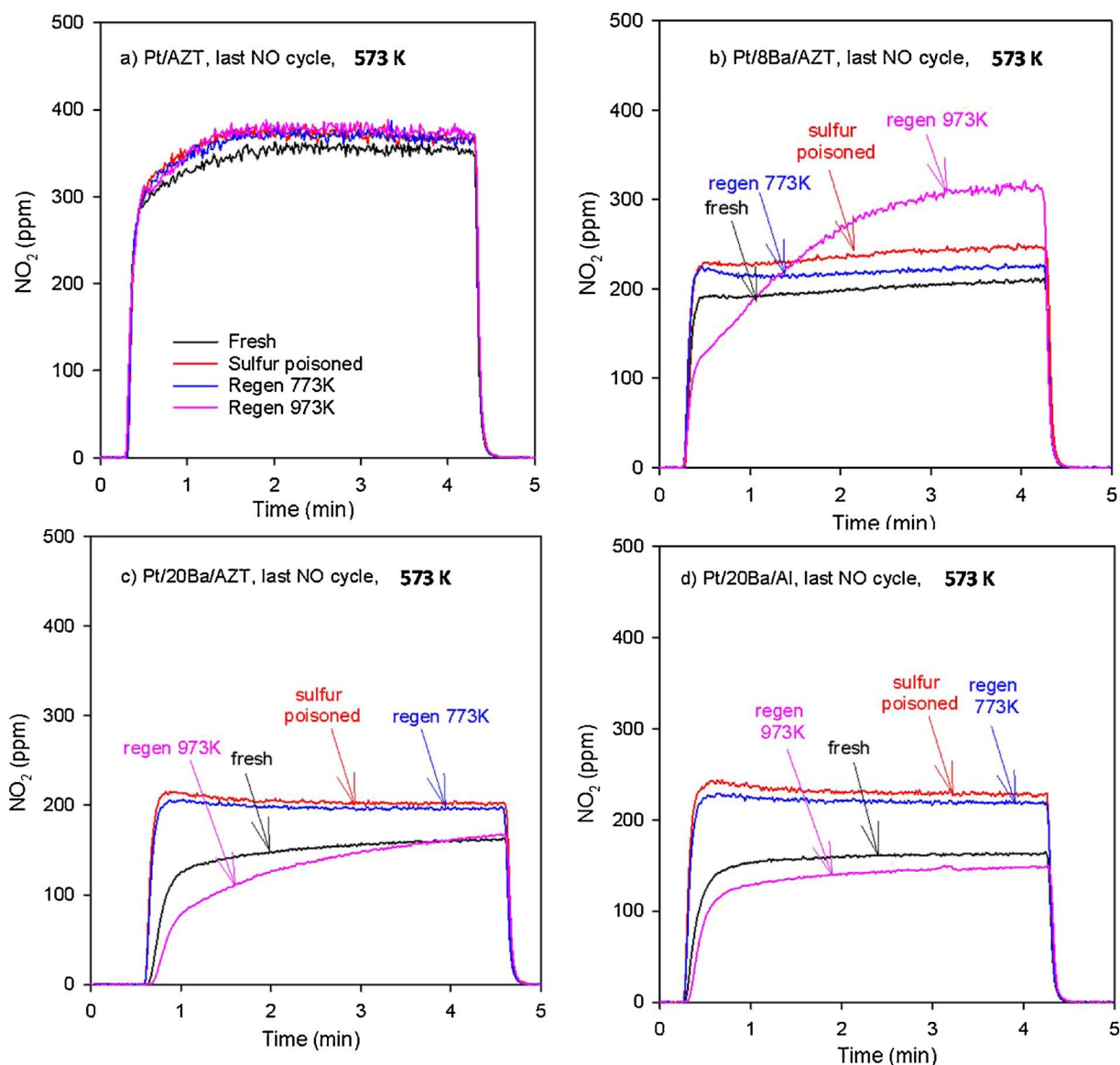
Fig. 6. NO oxidation to form NO_2 at 573 K during the last NO cycle for fresh, sulfur poisoned, 773 K-regenerated at and 973 K-regenerated catalystsfor a) Pt/AZT, b) Pt/8Ba/AZT, c) Pt/20Ba/AZT and d) Pt/20Ba/Al.

Fig. 5 for the fresh catalyst (black spectrum) revealed a main feature at 2052 cm^{-1} which can be ascribed to linear (atop) Pt^0-CO species [48–50]. For the spent catalyst (red spectrum) this peak was observed to shift to a higher frequency of 2059 cm^{-1} with a distinguishable tail towards lower frequencies, exhibiting a shoulder at 1966 cm^{-1}. The blue shift in the linear (atop) Pt^0-CO species in the spent catalyst can be readily ascribed to sintering and Pt particle size growth and increase in the extension of the Pt(111) facets/terraces on Pt nanoparticles. This argument is in good agreement with the observation of the shoulder at 1966 cm^{-1} for the spent catalyst which can be attributed to bridging CO species on Pt^0 sites located on the sintered Pt nanoparticles [48–50].

The NO oxidation is known to be important for NO_x storage when using NO as inlet feed. The NO oxidation is both a function of the amount of active sites, but it is also a structure-sensitive reaction, where larger Pt particles are more active for NO oxidation [51,52]. Moreover, Olsson and Fridell [52] found that sulfur poisoning followed by sulfur regeneration with hydrogen siginficantly improved the NO oxidation. In Fig. 6, the NO oxidation to NO_2 for the fresh, sulfur poisoned and regenerated catalysts are shown. Pt/AZT (Fig. 6a) exhibit very high NO oxidation activity for all samples and quite similar for all cases. Interestingly, for all other samples the NO oxidation capacity was higher

after sulfur poisoning. It should be remembered that in all these experiments lean-rich cycling was conducted after the sulfur poisoning. This means that the catalyst during the cycling was exposed to hydrogen in the rich phase and in addition to hydrogen during the pretreatment (at 773 K with 1% H_2, 5% CO_2 and 5% H_2O for 15 min) which was conducted before experiment at each temperature, which will remove some of the sulfur from the noble metal sites, and thereby facilitate the NO oxidation. Interestingly, the NO oxidation is quite different after sulfur regeneration at 973 K between the samples. For Pt/8BaO/AZT the NO_2 formation is significantly increased compared to all samples. This could be due to sintering and that larger Pt particles are more active compared to small Pt particles [53]. This increased NO_2 production can explain the larger NO_x storage observed after sulfur regeneration (see Fig. 4). However, for the Pt/20BaO/AZT and Pt/20BaO/Al, the NO oxidation activity went down after the 973 K regeneration and the reason for this could be that even though the larger Pt particles are more active, sintering is also decreasing the amount of active sites. These results clearly show that the noble metal activity for NO oxidation cannot explain the increase in NO_x storage for the sulfur regenerated samples at 973 K.

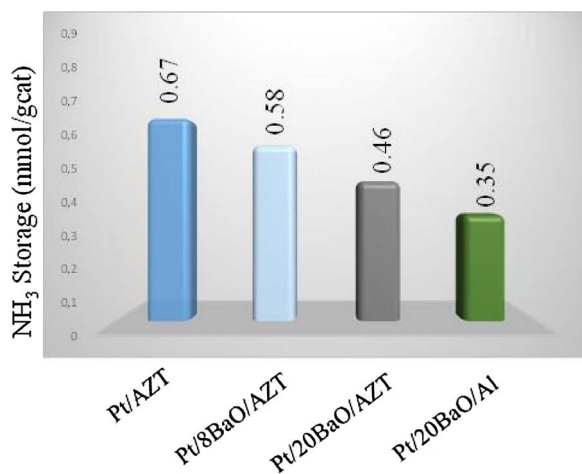In order to further elucidate the effect of high temperature sulfur
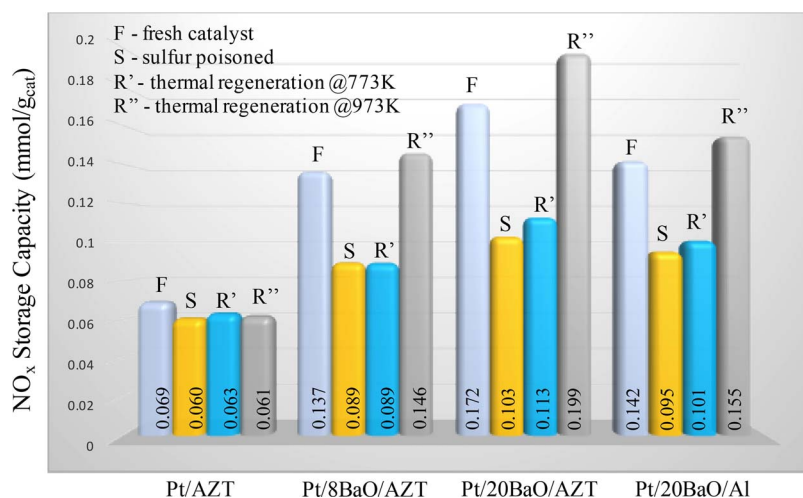
Fig. 7. NO_x storage capacities (NSC) of Pt/AZT, Pt/8BaO/AZT, Pt/20BaO/AZT and Pt/20BaO/Al monolithic catalysts at 573 K obtained in a flow-reactor using an inlet gas feed of 500 ppm NO_2, 5% O_2, 5% CO_2, 5% H_2O, balanced in Ar. F = fresh, S = SO_x poisoned, R' = regenerated at 773 K after SO_x poisoning, R" = regenerated at 973 K after SO_x poisoning (see text for details).

regeneration with hydrogen, the NO_x storage for the four catalysts when using NO_2 as inlet NO_x source is displayed in Fig. 7. In general, the NO_x storage is higher for the case with NO_2 in the inlet feed gas (compare Figs. 4 and 7), which is also observed at 573 K by Fridell *et al.* [54]. When using NO_2 in the feed the NO_x can store directly on the storage sites [55]. Interestingly, also for the case with NO_2 in the inlet feed the NO_x storage is higher after sulfur regeneration at 973 K for all barium containing catalysts, thus we suggest that there are morphological changes in the surface structure of the BaO/AZT mixed oxide system and Ba/Al system after sulfur poisoning and high temperature regeneration.

As discussed in detail in one of our recent reports, some of the trends in the NSC presented in Figs. 3 and 4 can be explained in the light of the relatively higher surface acidity of the AZT-supported materials as compared to the Pt/20BaO/Al benchmark catalyst. This is in agreement with the NH₃ uptake data as shown in Fig. 8 revealing ammonia storage quantities of 0.67, 0.58, 0.46 and 0.35 mmol/g_{cat} for Pt/AZT, Pt/8BaO/AZT, Pt/20BaO/AZT, and Pt/20BaO/Al; respectively [40]. These results are in very good accordance with the former pyridine adsorption FTIR experiments which revealed a higher surface concentration of Lewis acid sites for AZT-supported materials as compared to other Al_2O_3-based counterparts [40].

Relative changes in NSC values upon SO_x poisoning and subsequent regeneration for all of the investigated materials as compared to their

Table 2
Numerical values for NSC loss upon SO_x poisoning and NSC recovery after H_2-regeneration derived from data given in Figs. 4 and 5.

Catalyst Name and @ temperature	NSC Loss by poisoning (%)	Recovery after regeneration (%)
Pt/AZT @473 K	2.8	97.2
Pt/8BaO/AZT @473 K	8	96
Pt/20BaO/AZT @473 K	39.4	73.6
Pt/20BaO/Al @473 K	52	52
Pt/AZT @573 K	8.3	95.8
Pt/8BaO/AZT @573 K	34	71.6
Pt/20BaO/AZT @573 K	50	61.6
Pt/20BaO/Al @573 K	30.6	72.5

fresh forms are summarized in Table 2. These results suggest that regenerated Pt/8BaO/AZT catalyst reveals promising performance both at low (*i.e.* 473 K) and moderate (*i.e.* 573 K) temperatures surpassing the conventional Pt/20BaO/Al_2O_3 benchmark catalyst.

In-situ FTIR experiments were also performed in batch-mode on powder catalysts in order to investigate the relative extent of residual SO_x species remaining on the catalyst surfaces after SO_x poisoning and subsequent regeneration with H_2 (Fig. 9). These experiments reveal
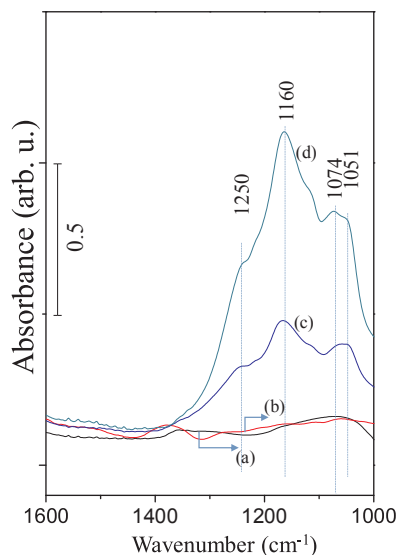

Fig. 8. NH₃ storage capacities of Pt/AZT, Pt/8BaO/AZT, Pt/20BaO/AZT and Pt/20BaO/Al monolithic catalysts derived from the integration of the corresponding NH₃-TPD curves. Prior to the NH₃-TPD analysis, all samples were exposed to 2000 ppm NH₃ at 323 K for 8 h followed by Ar(g) flow for 30 min at 323 K.

Fig. 9. *In-situ* FTIR spectra acquired after H_2-regeneration (773 K) of SO_x-poisoned catalysts at 673 K illustrating the residual sulfur species on (a) Pt/AZT, (b) Pt/8BaO/AZT, (c) Pt/20BaO/AZT and (d) Pt/20BaO/Al catalysts.
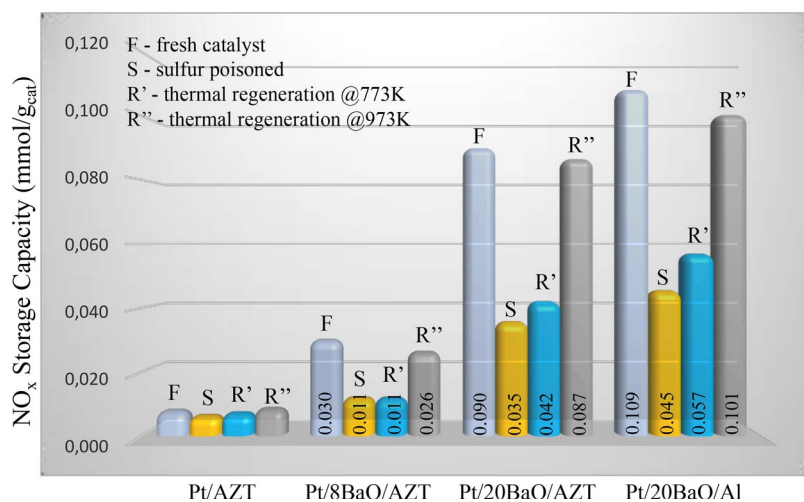
Fig. 10. NO_x storage capacities (NSC) of Pt/AZT, Pt/8BaO/AZT, Pt/20BaO/AZT and Pt/20BaO/Al monolithic catalysts at 673 K obtained in a flow-reactor using an inlet gas feed of 500 ppm NO, 5% O_2, 5% CO_2, 5% H_2O, balanced in Ar. F = fresh, S = SO_x poisoned, R = regenerated at 773 K after SO_x poisoning and R" = regenerated after SO_x poisoning (see text for details).

typical IR features corresponding to various surface and bulk sulfates/sulfite species as discussed in more depth in our former reports [9,40]. It is apparent in Fig. 9 that due to its weaker acidity (Fig. 8), conventional Pt/20BaO/Al catalyst retains the greatest amount of SO_x species among all other catalysts after identical set of sulfur poisoning and regeneration steps. On the other hand, significantly more acidic Pt/AZT and Pt/8BaO/AZT catalysts can get rid of almost all of the SO_x species after regeneration with H_2. However, these latter catalysts, in turn, suffer from limited NSC due to their higher acidity. It is worth mentioning that all of the investigated catalysts including Pt/AZT and Pt/8BaO/AZT uptake different extents of SO_x species upon $SO_2 + O_2$ adsorption as described in detail in one of our former reports [40]. Along these lines, Pt/20BaO/AZT catalyst seems to possess a more favourable trade-off between NSC (Figs. 3 and 4) and sulfur tolerance (Fig. 9), revealing acidic-enough character (Fig. 8) to enable efficient sulfur regeneration without experiencing a severe suppression in NSC.

NSC measurements performed at high temperatures such as 673 K (Fig. 10) illustrate that, stability of nitrates significantly decreases on the more acidic surfaces (Pt/AZT and Pt/8BaO/AZT) which significantly suffer from loss of NSC. Fig. 10 clearly highlights the need for the improvement of the NSC of AZT-based catalysts at elevated temperatures so that they can surpass the performance of conventional Pt/20BaO/Al benchmark catalyst.

Integrated ammonia production from the cycling experiments are shown in Fig. 11, for 473, 573 and 673 K. Ammonia production during rich conditions could be beneficial, if it is used in combination with an SCR unit [56]. For example, during vehicle chassis dynamometer experiments performed by Volvo Cars an SCR catalyst was used downstream of the LNT [57].

These corresponding results in general lead us to conclude that ammonia production over fresh materials increases along with the increase in temperature. Ammonia production over platinum in Pt/SiO$_2$ was previously found to increase with temperature [58], which is in line with our results. However, this general trend was not applicable for both Pt/8BaO/AZT and Pt/20BaO/AZT samples at 673 K. This is because ammonia production over NO_x storage materials is very complex. It mainly relates to three parts: (i) formation of ammonia from the inlet NO_x over the Pt sites, (ii) formation of ammonia from the stored NO_x, which is being released in the rich phase and (iii) consumption of ammonia due to SCR reaction with the stored NO_x, which will lower the amount of ammonia after the catalyst [59,60]. This means that the stored NO_x can increase the ammonia formation because of increased availability of NO_x, but also decrease the ammonia production due to the SCR reaction. The selectivity between these two reactions depend on the catalyst material, such as proximity between the noble metal and storage component, noble metal particle activity, *etc*. For the Pt/

20BaO/Al$_2$O$_3$ material the ammonia production increases for all temperatures. Fig. S1, Supplementary material shows the ammonia profile. At 473 K, there is a sharp and quite small ammonia peak when switching to rich conditions, which is due to small amounts of stored NO_x. Quickly, the ammonia peaks levels off to close to 500 ppm which is the inlet NO level. These results show that a clear limiting factor is the supply of NO_x. When increasing the temperature using NO in the inlet feed, the ammonia production is increasing due to increased conversion of the stored NO_x to ammonia. Indeed, the NO_x storage is higher for 673 K compared to 573 K and compared to 473 K (compare Figs. 10, 4 and 3). This means that the ammonia production from the released NO_x is increasing more compared to the SCR reactions (which also are increasing with temperature), resulting in increased selectivity for ammonia.

For Pt/20BaO/AZT, the ammonia production decreases at the highest temperature (673 K), see Figs. 11 and S2, Supplementary material. The reason for this is that the NO_x storage is quite similar at 673 K and 573 K for this material and the increased temperature increases the rate for the SCR reaction more, which resulted in less ammonia in the outlet. For the Pt/BaO/Al$_2$O$_3$ on the other hand, the NO_x storage was substantially increased at 673 K, which resulted in much larger availability of NO_x and resulted in an overall increased ammonia concentration even though SCR rate was faster.

Examining the results for sulfur poisoning and regeneration at 473 K (see Fig. 11a) the ammonia production for fresh and sulfur poisoned catalysts is quite similar, except for the Pt/20BaO/Al$_2$O$_3$ sample, where a significant decrease is seen. For the Pt/20BaO/Al$_2$O$_3$ catalyst, most of the ammonia production could be regenerated, but it required high temperature (973 K). At 573 K (see Fig. 11b), the sulphur poisoning results in lower ammonia production, but most of it could be regained after regeneration. Also at 673 K, sulphur poisoning was clear (see Fig. 11c), however the ammonia production capacity could not be fully regained. At 673 K, the NO_x storage capacity is not either fully regained after the 973 K regeneration, which means that there is less stored NO_x on the catalysts, and thereby less available NO_x for the ammonia production and this can explain why the ammonia production could not be fully regained after the regeneration.

Interestingly, the ammonia production was higher for the AZT containing samples after sulfur regeneration compared to fresh material. These results are in line with the NO_x storage results presented in Figs. 3 and 4 and the reason for this could be structural changes in the materials after sulfur poisoning followed by regeneration in the presence of hydrogen at high temperatures.

The N$_2$O production is shown in Fig. 12 for the three temperatures. It is observed that the N$_2$O production is significantly higher at low temperature, which is in line with the study by Lindholm *et al.* [61].
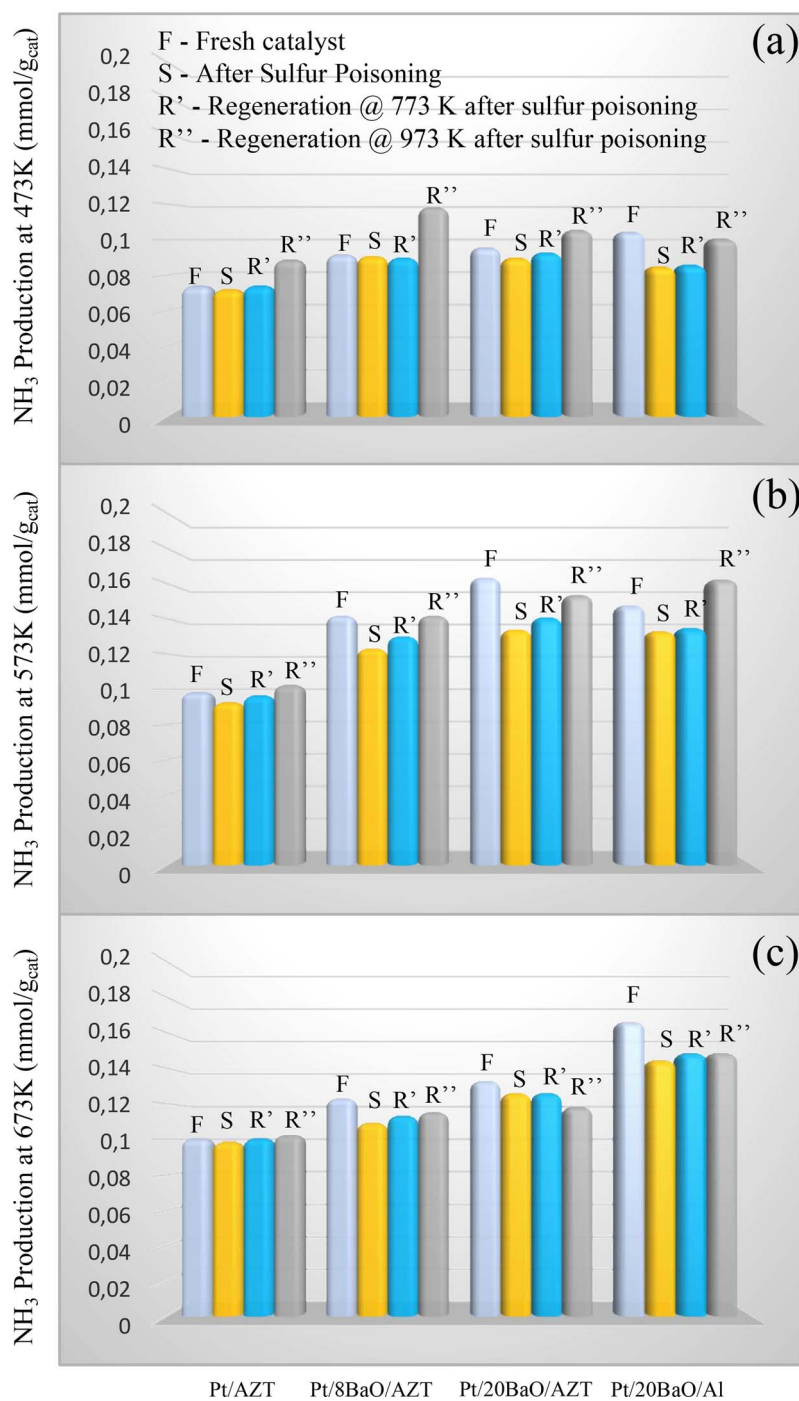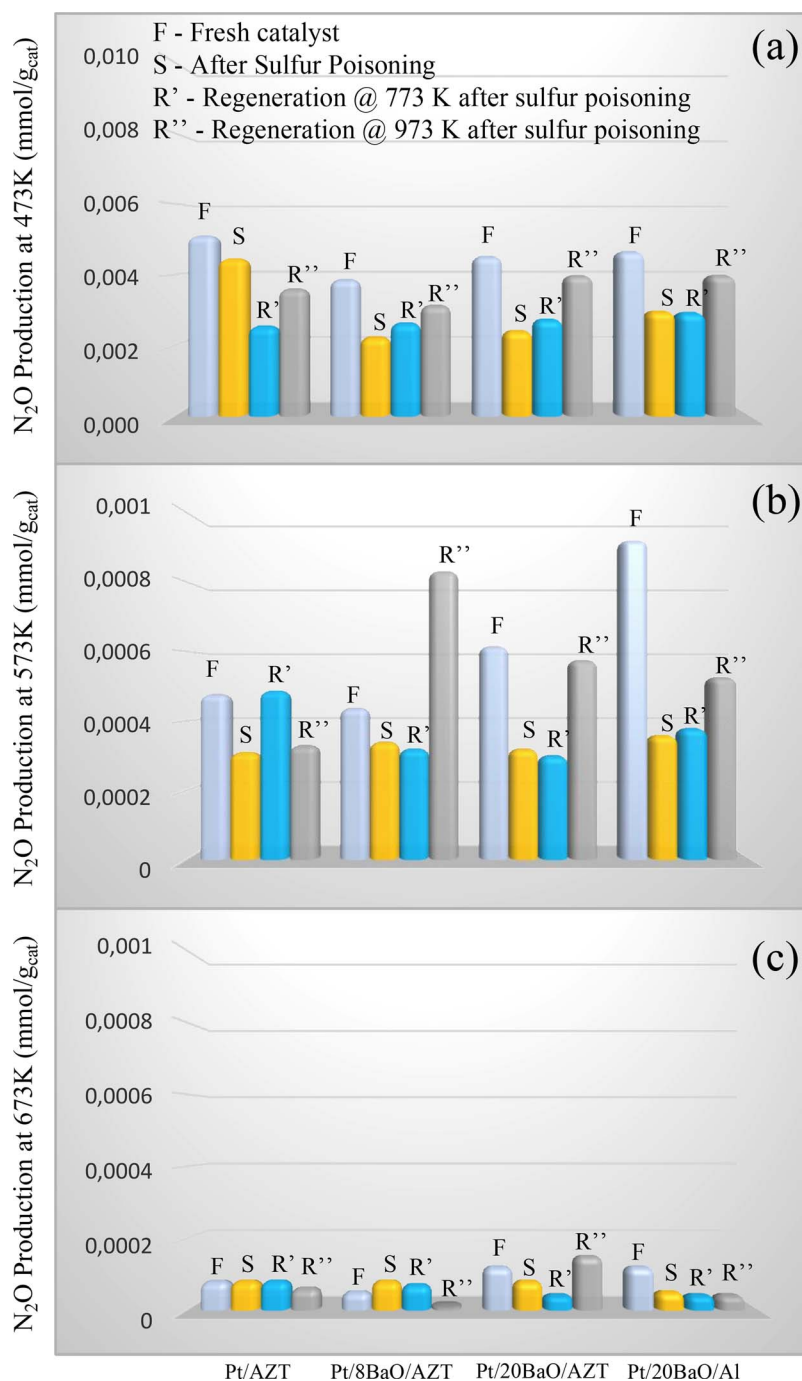
Fig. 11. Ammonia production for Pt/AZT, Pt/8BaO/AZT, Pt/20BaO/AZT and Pt/20BaO/Al monolithic catalysts at a) 473 K, b) 573 K and c) 673 K obtained in a flow-reactor using an inlet gas feed of 500 ppm NO, 5% O_2, 5% CO_2, 5% H_2O, balanced in Ar. F = fresh, S = SO_x poisoned, R' = regenerated at 773 K after SO_x poisoning and R" = regenerated at 973 K after SO_x poisoning (see text for details).

Interestingly, the fresh Pt/BaO/AZT materials showed lower N_2O formation compared to Pt/BaO/Al_2O_3 at 573 K, which is very beneficial. Simultaneously, the Pt/BaO/AZT produced more ammonia, and the lower N_2O formation for Pt/BaO/AZT is likely related to higher selectivity for the formation of ammonia compared to N_2O. Moreover, at 473 K (see Fig. 12a) there is a clear poisoning effect of the N_2O formation for all barium containing samples and most of the N_2O production could be restored after regeneration. At 573 K, poisoning was also observed, but the regeneration capability varied between the samples. However, at the highest temperature (*i.e.* 673 K) the N_2O production was between 38 and 86 times lower compared to at 473 K

and due to this low amount, no clear trends could be visible.

We also performed preliminary experiments in order to demonstrate that high-temperature NSC of AZT-based materials can be improved further by utilizing multiple NO_x-storage components where one of these components provide efficient NSC at T ≤ 573 K, while the second component enables NSC at elevated temperatures (*i.e.* 673 K). K_2O is a versatile NO_x storage component used in NSR/LNT catalysts at high temperatures [62,63]. Therefore, currently observed NSC loss at high temperatures, particularly for Pt/8BaO/AZT could be alleviated by incorporating a high-temperature NO_x storage functionality (*i.e.* K_2O) to the catalyst formulation as shown in Fig. 13. Fig. 13 shows NSC for

Fig. 12. N$_2$O production for Pt/AZT, Pt/8BaO/AZT, Pt/20BaO/AZT and Pt/20BaO/Al monolithic catalysts at a) 473 K, b) 573 K and c) 673 K obtained in a flow-reactor using an inlet gas feed of 500 ppm NO, 5% O$_2$, 5% CO$_2$, 5% H$_2$O, balanced in Ar. F = fresh, S = SO$_x$ poisoned, R = regenerated at 773 K after SO$_x$ poisoning and R" = regenerated at 973 K after SO$_x$ poisoning (see text for details).

monolithic catalysts in their fresh forms which only contained K$_2$O (Pt/ 5.4 K$_2$O/AZT) or BaO (Pt/8BaO/AZT) as storage domains as well as a hybrid catalyst comprised of a physical (50 wt.%) mixture of Pt/5.4 K$_2$O/AZT – Pt/8BaO/AZT. Preliminary results in Fig. 13 clearly indicate that NSC of the fresh Pt/8BaO/AZT can be improved at all of the investigated temperatures (*i.e.* 473–673 K) by physically mixing it with Pt/5.4 K$_2$O/AZT. In our forthcoming studies, this strategy will be applied to other AZT-based LNT catalysts (including Pt/20BaO/AZT) in order to present a comprehensive report on the catalytic behaviour and the surface chemistry of the NO$_x$/SO$_x$ species on these advanced hybrid catalytic architectures.

In order to shed a light on the preliminary NSC results given in

Fig. 13, we performed *in-situ* FTIR experiments and investigated NO$_2$ adsorption on Pt/8BaO/AZT, (b) Pt/5.4 K$_2$O/AZT – Pt/8BaO/AZT (physical mixture), and Pt/5.4K$_2$O/AZT powder catalysts as illustrated in Fig. 14. While the majority of the adsorbed NO$_x$ species on Pt/8BaO/ AZT corresponded to surface nitrates and nitrites (evident by the IR vibrational frequencies located at 1609, 1575, 1460, 1298 and 1241 cm^{-1}), K$_2$O incorporation significantly altered the nature of the existing NO$_x$ species, favouring the formation of bulk-like nitrates on K$_2$O domains characterized by IR features at 1396 and 1369 cm^{-1} as well as the surface-like nitrates [64–66]. These interesting *in-situ* FTIR results are consistent with the fact that incorporation of K$_2$O domains extends of the operational temperature window towards higher
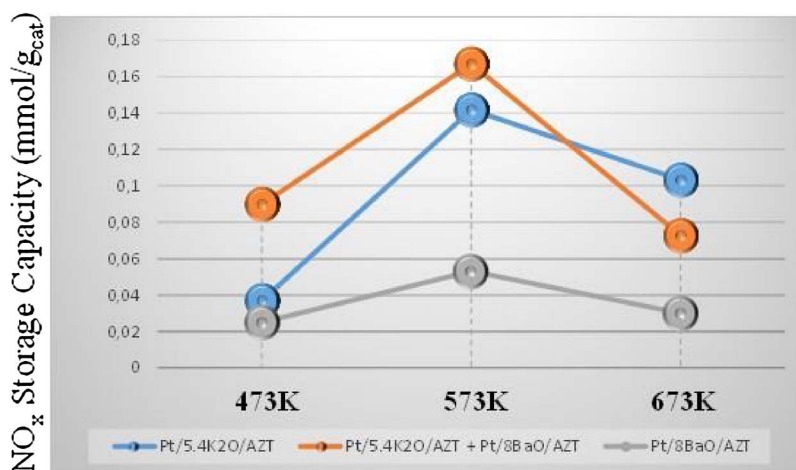
Fig. 13. NO_x storage capacities (NSC) of fresh Pt/5.4 K_2O/AZT, Pt/5.4 K_2O/AZT – Pt/8BaO/AZT (physical mixture) and Pt/8BaO/AZT monolithic catalysts via flow-reactor experiments at 673 K with an inlet gas feed of 500 ppm NO, 5% O_2, 5% CO_2, 5% H_2O, balanced in Ar.
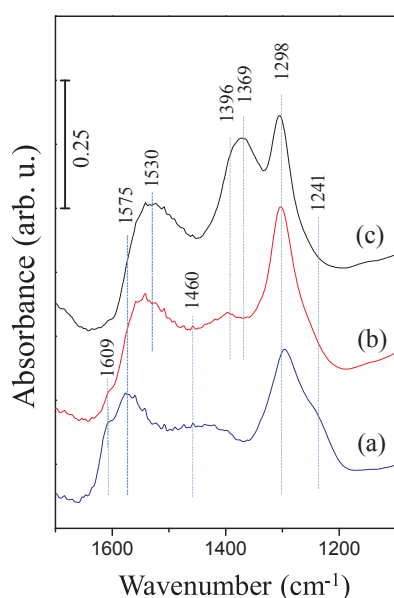

Fig. 14. *In-situ* FTIR spectra acquired at 673 K after NO_2 saturation of (a) Pt/8BaO/AZT, (b) Pt/5.4 K_2O/AZT- Pt/8BaO/AZT (physical mixture) and (c) Pt/5.4 K_2O/AZT powder catalysts.

temperatures by enabling the formation of a greater amount of thermally stable bulk-like nitrates.

4. Conclusions

Al_2O_3/ZrO_2/TiO_2 (AZT) ternary mixed oxides functionalized with Pt and BaO were synthesized in powder and monolithic forms and were utilized in NO_x Storage Reduction/Lean NO_x Trap (NSR/LNT) catalysis as alternative catalytic materials. Adsorption of NO_x and SO_x species and their interactions with the catalyst surfaces were systematically investigated *via in-situ* FTIR technique revealing different NO_x co-ordination geometries governed by the presence and the loading of BaO in the powder catalyst formulation. While BaO-free Pt/AZT stored NO_x as surface nitrates, BaO incorporation also led to the formation of bulk-like ionic nitrate species. NO_x adsorption results obtained from the current Temperature Programmed Desorption (TPD) data indicated that NO_x Storage Capacity (NSC) was enhanced due to BaO incorporation into the powder catalyst and NSC was found to increase in the following order: Pt/AZT < Pt/8BaO/AZT < Pt/20BaO/Al_2O_3 < Pt/20BaO/AZT. Increase in the NSC with increasing BaO loading was found to be

at the expense of the formation of bulk-like sulfates after SO_x exposures. These bulk-like sulfates were observed to require higher temperatures for complete regeneration with H_2(g). Catalytic activity results obtained *via* flow reactor tests with monolithic catalysts suggested that Pt/AZT and Pt/8BaO/AZT catalysts with stronger surface acidity also revealed higher resistance against sulfur poisoning and superior SO_x regeneration on the NSC capacity at 473 K and 573 K in spite of their relatively lower NSC. Monolithic Pt/20BaO/AZT catalyst revealed superior NSC with respect to the conventional Pt/20BaO/Al_2O_3 benchmark catalyst at 573 K after sulfur regenerations. On the other hand, this trend was reversed at high-temperatures (*i.e.* 673 K). Interestingly after sulfur poisoning and high temperature regeneration at 973 K with hydrogen, the NSC at especially 573 K increased and was significantly higher for several cases compared to the fresh catalyst. This can be related to the structural changes in the materials after high temperature reduction and this behavior was the strongest for the materials containing both BaO and AZT.

Preliminary results were presented demonstrating the enhancement of the high-temperature NSC of AZT-based materials by exploiting multiple NO_x-storage components where BaO functioned as the low/mid-temperature NO_x-storage domain and K_2O served as the high-temperature NO_x storage domain. Enhancement in the high-temperature NO_x-storage in the BaO-K_2O multiple storage domain systems was attributed to the formation of additional thermally stable bulk-like nitrates upon K_2O incorporation.

Appendix A. Supplementary data

Supplementary data associated with this article can be found, in the online version, at https://doi.org/10.1016/j.cattod.2018.01.028.

References

[1] OECD, Environment at a Glance 2015: OECD Indicators, OECD Publishing, Paris, 2015https://doi.org/10.1787/9789264235199-en.
[2] N. Myioshi, S. Matsumoto, K. Katoh, T. Tanaka, K. Harada, N. Takahashi, K. Yokota,

M. Sugiura, K. Kasahara, SAE Technical Papers Series, 1995, 950809.

[3] S. Roy, A. Baiker, Chem. Rev. 109 (2009) 4054–4091.
[4] W.S. Epling, L.E. Campbell, A. Yezerets, N.W. Currier, J.E. Parks, Catal. Rev. 46 (2004) 163–245.
[5] M. Weibel, N. Waldbüsser, R. Wunsch, D. Chatterjee, B. Bandl-Konrad, B. Krutzsch, Top. Catal. 52 (2009) 1702–1708.
[6] J. Wang, Y. Ji, G. Jacobs, S. Jones, D.J. Kim, M. Crocker, Appl. Catal. B 148–149 (2014) 51–61.
[7] P. Forzatti, L. Lietti, Catal. Today 155 (2010) 131–139.
[8] Z. Say, E.I. Vovk, V.I. Bukhtiyarov, E. Ozensoy, Top. Catal. 56 (2013) 950–957.
[9] G.S. Senturk, E.I. Vovk, V.I. Zaikovskii, Z. Say, A.M. Soylu, V.I. Bukhtiyarov, E. Ozensoy, Catal. Today 184 (2012) 54–71.
[10] N. Takahashi, H. Shinjoh, T. Iijima, T. Suzuki, K. Yamazaki, K. Yokota, H. Suzuki, N. Miyoshi, S. Matsumoto, T. Tanizawa, T. Tanaka, S. Tateishi, K. Kasahara, Catal. Today 27 (1996) 63–69.
[11] C. Sedlmair, K. Seshan, A. Jentys, J.A. Lercher, Catal. Today 75 (2002) 413–419.
[12] J.R. Theis, Catal. Today 267 (2016) 93–109.
[13] L. Lietti, J. Catal. 60 (2005) 265–275.
[14] P. Engström, A. Amberntsson, M. Skoglundh, E. Fridell, G. Smedler, Appl. Catal. B Environ. 22 (1999) 241–248.
[15] S. Elbouazzaoui, E.C. Corbos, X. Courtois, P. Marecot, D. Duprez, Appl. Catal. B Environ. 61 (2005) 236–243.
[16] X. Wang, Y. Yu, H. He, Appl. Catal. B: Environ. 104 (2011) 151–160.
[17] M. Yang, Y. Li, J. Wang, M. Shen, J. Catal. 271 (2010) 228–238.
[18] Z. Say, E.I. Vovk, V.I. Bukhtiyarov, E. Ozensoy, Appl. Catal. B: Environ. 142–143 (2013) 89–100.
[19] R. Hummatov, D. Toffoli, O. Gulseren, E. Ozensoy, H. Ustunel, J. Phys. Chem. C 116 (2012) 6191–6199.
[20] S.M. Andonova, G.S. Senturk, E. Kayhan, E. Ozensoy, J. Phys. Chem. C 113 (2009) 11014–11026.
[21] S.M. Andonova, G.S. Senturk, E. Ozensoy, J. Phys. Chem. C 114 (2010) 17003–17016.
[22] M. Piacentini, M. Maciejewski, A. Baiker, Appl. Catal. B: Environ. 66 (2006) 126–136.
[23] M. Piacentini, M. Maciejewski, T. Burgi, A. Baiker, Top. Catal. 30–31 (2004) 71–80.
[24] T. Ozaki, T. Masui, K. Machida, G. Adachi, T. Sakata, H. Mori, Chem. Mater. 12 (2000) 643–649.
[25] J.C. Jiang, X.Q. Pan, G.W. Graham, R.W. McCabe, J. Schwank, Catal. Lett. 53 (1998) 37–42.
[26] J. Kaspar, P. Fornasiero, N. Hickey, Catal. Today 77 (2003) 419–449.
[27] L.F. Liotta, A. Macaluso, G.E. Arena, M. Livi, G. Centi, G. Deganello, Catal. Today 75 (2002) 439–449.
[28] M. Eberhardt, R. Riedel, U. Gobel, J. Theis, E.S. Lox, Top. Catal. 30–31 (2004) 135–142.
[29] M. Casapu, J.D. Grunwaldt, M. Maciejewski, M. Wittrock, U. Gobel, A. Baiker, Appl. Catal. B: Environ. 63 (2006) 232–242.
[30] K. Ito, S. Kakino, K. Ikeue, M. Machida, Appl. Catal. B: Environ. 74 (2007) 137–143.
[31] T. Kanazawa, Catal. Today 96 (2004) 171–177.
[32] B.M. Reddy, A. Khan, Catal. Rev. 47 (2005) 257–296.
[33] K. Arata, K. Akutagawa, Bull. Tanabe, Chem. Soc. Jpn. 49 (1976) 390–393.
[34] I. Wang, W.F. Chang, R.J. Shiau, J.C. Wu, C.S. Chung, J. Catal. 83 (1983) 428–436.

[35] H. Imagawa, N. Takahashi, T. Tanaka, S. Matsunaga, H. Shinjoh, Appl. Catal. B: Environ. 92 (2009) 23–29.
[36] H. Imagawa, T. Tanaka, N. Takahashi, S. Matsunaga, A. Suda, H. Shinjoh, Appl. Catal. B: Environ. 86 (2009) 63–68.
[37] Z.Q. Zou, M. Meng, X.Y. Zhou, X.G. Li, Y.Q. Zha, Catal. Lett. 128 (2009) 475–482.
[38] S.P. Del Valle, O. Marie, H.P. Nguyen, Appl. Catal. B: Environ. 223 (2018) 116–124.
[39] Z. Say, M. Tohumeken, E. Ozensoy, Catal. Today 231 (2014) 135–144.
[40] Z. Say, O. Mihai, M. Tohumeken, K.E. Ercan, L. Olsson, E. Ozensoy, Catal. Sci. Technol. 7 (2017) 133–144.
[41] T. Szailer, J.H. Kwak, D.H. Kim, J. Szanyi, C. Wang, C.H.F. Peden, Catal. Today 114 (2006) 86–93.
[42] I.S. Pieta, M. García-Diéguez, C. Herrera, M.A. Larrubia, L.J. Alemany, J. Catal. 270 (2010) 256–267.
[43] M. Kantcheva, Appl. Catal. B: Environ. 42 (2003) 89–109.
[44] M. Kantcheva, A.S. Vakkasoglu, J. Catal. 223 (2004) 352–363.
[45] Z. Say, M. Dogac, E.I. Vovk, Y.E. Kalay, C.H. Kim, W. Li, E. Ozensoy, Appl. Catal. B Environ. 154–155 (2014) 51–61.
[46] D.H. Kim, J.H. Kwak, J. Szanyi, S.D. Burton, C.H.F. Peden, Appl. Catal. B Environ. 72 (2007) 233–239.
[47] T. Szailer, J.H. Kwak, D.H. Kim, J.C. Hanson, C.H.F. Peden, J. Szanyi, J. Catal. 239 (2006) 51–64.
[48] P.A. Carlsson, L. Osterlund, P. Thormählen, A. Palmqvist, E. Fredell, J. Jansson, M. Skoglundh, J. Catal. 226 (2004) 422–434.
[49] M. Primet, J.M. Basset, M.V. Mathieu, M. Prettre, J. Catal. 29 (1973) 213.
[50] M.J. Kale, P. Christopher, ACS Catal. 6 (2016) 5599–5609.
[51] L. Olsson, H. Karlsson, Catal. Today 147S (2009) S290–S294.
[52] L. Olsson, E. Fridell, J. Catal. 210 (2002) 340–353.
[53] X. Auvray, T. Pingel, E. Olsson, L. Olsson, Appl. Catal. B: Environ. 129 (2013) 517–527.
[54] E. Fridell, M. Skoglundh, B. Westerberg, S. Johansson, G. Smedler, J. Catal. 183 (1999) 196–209.
[55] L. Olsson, H. Persson, E. Fridell, M. Skoglundh, B. Andersson, J. Phys. Chem. B 105 (2001) 6895–6906.
[56] A. Lindholm, H. Sjövall, L. Olsson, Appl. Catal. B: Environ. 98 (2010) 112–121.
[57] J.d.A. Goes, L. Olsson, M. Berggrund, A. Kristoffersson, L. Gustafson, M. Hicks, SAE Int. J. Engines 10 (4) (2017) 1613–1626.
[58] A. Lindholm, N.W. Currier, A. Yezerets, L. Olsson, Top. Catal. 42–43 (2007) 83–89.
[59] A. Lindholm, N.W. Currier, J.H. Li, A. Yezerets, L. Olsson, J. Catal. 258 (2008) 273–288.
[60] W.P. Partridge, J.S. Choi, Appl. Catal. B: Environ. 91 (2009) 144–151.
[61] A. Lindholm, N.W. Currier, E. Fridell, A. Yezerets, L. Olsson, Appl. Catal. B: Environ. 75 (2007) 78–87.
[62] M. Takeuchi, S. Matsumoto, Top. Catal. 28 (2004) 151–156.
[63] T.J. Toops, D.B. Smith, W.P. Partridge, Catal. Today 114 (2006) 112–124.
[64] D.H. Kim, K. Mudiyanselage, J. Szanyi, J.C. Hanson, C.H.F. Peden, J. Phys. Chem. C 118 (2014) 4189–4197.
[65] F. Prinetto, M. Manzoli, S. Morandi, F. Frola, G. Ghiotti, J. Phys. Chem. C 114 (2010) 1127–1130.
[66] L. Righini, F. Gao, L. Lietti, J. Szanyi, C.H.F. Peden, Appl. Catal. B Environ. 181 (2015) 862–873.